A MINI element over star convex polytopes

Amrita Francis[a], Alejandro Ortiz-Bernardin[b,c], Stéphane PA Bordas[d,e,1,*], Sundararajan Natarajan[a]

[a] *Integrated Modelling and Simulation Lab, Department of Mechanical Engineering, Indian Institute of Technology Madras, Chennai-600036, India.*
[b] *Department of Mechanical Engineering, Universidad de Chile, Av. Beauchef 851, Santiago 8370456, Chile.*
[c] *Computational and Applied Mechanics Laboratory, Center for Modern Computational Engineering, Facultad de Ciencias Físicas y Matemáticas, Universidad de Chile, Av. Beauchef 851, Santiago 8370456, Chile.*
[d] *Faculté des Sciences, de la Technologie et de la Communication, University of Luxembourg, Luxembourg.*
[e] *Institute of Research and Development, Duy Tan University, K7/25 Quang Trung, Danang, Vietnam.*

Abstract

In this paper, we extend the concept of MINI element over triangles to star convex arbitrary polytopes. This is achieved by employing the volume averaged nodal projection (VANP) method over polytopes in combination with the strain smoothing technique. Within this framework, the dilatation strain is projected onto the linear approximation space, thus resulting in a purely displacement based formulation. The stability is ensured by enhancing the displacement field with bubble basis functions. The salient features of the proposed method are two fold: the VANP alleviates the locking phenomenon and the strain smoothing suppresses the need to compute the derivative of the basis functions, thus reducing the computational burden. Various benchmark problems in two and three dimensions are numerically solved to demonstrate the robustness, accuracy and the convergence properties of the proposed framework.

Keywords: VANP operator, nearly-incompressible elasticity, bubble basis functions, strain smoothing (SFEM), arbitrary polytopes, volumetric locking.

1. Introduction

The introduction of elements with arbitrary edges and faces in two and three dimensions, respectively, has revolutionized and generalized the finite element method (FEM) and has led to the development of the polygonal FEM [1–4]. Some of the salient features of the PFEM are: (a) relaxes the restriction on element topology; (b) can work with non-conforming elements and quadtree/octree decomposition without splitting into simplex elements or using constraint equations [5] and (c) offers greater flexibility in meshing complex geometries [3, 6, 7] and in fracture problems [8]. However, one of the challenges faced with the PFEM is in evaluating the integral of the weak form exactly, which affects the accuracy of the results. The issue is basically due to lack of polynomial consistency of the discrete system causing

*Corresponding author
[1] Faculté des Sciences, de la Technologie et de la Communication, University of Luxembourg, Luxembourg.

a limit on the convergence of the finite element solutions [9, 10]. Thus, various efforts have been put to develop the quadrature scheme for the PFEM [10–12]. Inspired by the nodal integration scheme proposed for the meshfree methods [13–15] and later extended to the finite element method by Liu *et al.,* [16], Francis and Natarajan [17–19] employed the cell-based strain smoothing scheme for numerically integrating the terms in the bilinear and linear form.

Due to aforementioned properties, in the recent past, considerable effort has been made to develop methods with polygonal discretizations, viz., virtual element method [20–23], virtual node method [24], smoothed finite element method [18, 25], scaled boundary finite element method [17, 26, 27] and the discontinuous Galerkin method [28]. Since its inception, the PFEM has been employed to solve problems involving large deformations [29], contact problems [30] and fracture mechanics [8]. However, to the best of author's knowledge, only a few papers have employed polygonal finite element method for nearly incompressible elasticity [10, 31] and fluid flow [11]. Talischi *et al.,* [11] employed a linearly complete barycentric coordinates with piecewise constant pressure interpolation over Voronoi type meshes. It was shown that the formulation was unconditionally stable without any additional treatment. In their formulation, pressure was treated as additional variable, moreover, the pressure is discontinuous across the element boundaries.

The main objectives of the paper are: (a) to extend the recently proposed '*v*olume averaged nodal projection' (VANP) method to arbitrary polytopes (in both two and three dimensions) and (b) employ the cell-based strain smoothing technique to integrate the terms in the bilinear linear form. The VANP is a purely-displacement based formulation introduced by Ortiz *et al.,* [32–34]. Unlike the previous work, herein we present a pure displacement formulation using the VANP technique and consider both polygonal and polyhedral finite elements. Within this framework, the displacement field is approximated over the enhanced nodes with bubble basis function ensuring stability and the linearly complete pressure field is approximated over the standard nodes using Wachspress basis functions. The locking-free behavior of the VANP approach is rendered by projecting the dilatation strain onto the linear approximation space. Few other approaches of stabilized mixed formulation with lower-order elements and equal order interpolants using local L^2 projection for pressure are discussed in [35, 36] and the projection of the pressure field onto a lower space through a least-squares based projection technique are given in [37, 38]. The efficacy and robustness of the arbitrary polytopes in nearly incompressible regime are presented by solving few benchmark problems. The salient features of the work are:

- the VANP method alleviates locking phenomenon and is purely a displacement based formulation. The pressure is continuous across the element boundaries and computed in the post-processing step.
- the strain smoothing suppresses the need for isoparametric mapping and hence the computation of the Jacobian is eliminated.

The rest of the manuscript is organized as follows: Section 2 summarizes the formulation consisting of the strong form for the incompressible linear elastic isotropic material, the *u*-*p* mixed weak form, the construction of Wachspress basis functions and bubble basis functions and the VANP method. Section 4 consists of the two dimensional and three dimensional numerical examples to prove the efficiency and the convergence properties of the proposed framework, followed by the conclusions and future work.

2. Formulation

2.1. Strong Form

Consider an elastic body in $d = \{2, 3\}$ dimensional space defined by an open domain $\Omega \subset \mathbb{R}^d$, bounded by the d - 1 dimensional surface Γ such that $\Gamma = \Gamma_{\mathrm{u}} \cup \Gamma_{\mathrm{t}}$ and $\Gamma_{\mathrm{u}} \cap \Gamma_{\mathrm{t}} = \emptyset$. The governing equation with boundary conditions using mixed formulation for both incompressible and nearly-incompressible linear elastic isotropic material is described below:

$$\boldsymbol{\nabla} \cdot \boldsymbol{\sigma} + \mathbf{b} = \mathbf{0} \text{ in } \Omega \tag{1a}$$

$$\boldsymbol{\nabla} \cdot \mathbf{u} + \frac{p}{\lambda} = 0 \text{ in } \Omega \tag{1b}$$

$$\mathbf{u} = \overline{\mathbf{u}} \text{ on } \Gamma_u \tag{1c}$$

$$\boldsymbol{\sigma}.\mathbf{n} = \overline{\mathbf{t}} \text{ on } \Gamma_{\mathrm{t}} \tag{1d}$$

where $\mathbf{u}$ describes the nodal displacement of the elastic body subjected to external tractions $\overline{\mathbf{t}}$ and body force $\mathbf{b}$. The Γ_{u} is the Dirichlet boundary and Γ_{t} is the Neumann boundary. The Cauchy stress tensor $\boldsymbol{\sigma}$ is related to the small strain tensor $\boldsymbol{\varepsilon}$ and the pressure parameter p by the following constitutive relation:

$$\boldsymbol{\sigma}(\mathbf{u}, p) = -p\mathbf{I} + 2\mu\nabla\mathbf{u} \tag{2}$$

where λ and μ are the Lame's constant which are defined as:

$$\lambda = \frac{E\nu}{(1+\nu)(1-2\nu)} \tag{3}$$

$$\mu = \frac{E}{2(1+\nu)} \tag{4}$$

where ν is the Poisson's ratio and E is the Young's modulus of the material. The kinematic relation between the small strain tensor $\boldsymbol{\varepsilon}$ and the displacement vector $\mathbf{u}$ is:

$$\boldsymbol{\varepsilon} = \nabla\mathbf{u} = \frac{1}{2}\left(\nabla\mathbf{u} + \nabla\mathbf{u}^{\mathrm{T}}\right) \tag{5}$$

For nearly-incompressible linear elastic body, as ν tends to 0.5, the volumetric strain is zero, therefore we can say $\nabla.\mathbf{u} = \boldsymbol{\varepsilon}^{vol} = \mathrm{tr}(\boldsymbol{\varepsilon}) \approx 0$ Thus, the hydrostatic pressure field p can be approximate as :

$$p = -\lambda\nabla.\mathbf{u} = -\lambda\mathrm{tr}(\boldsymbol{\varepsilon}) = -\lambda\boldsymbol{\varepsilon}^{vol} \tag{6}$$

2.2. Weak Form

Let U and V be the trial and the test spaces for the displacement field, respectively, such that

$$U := \{\mathbf{u} : \mathbf{u} \in H^1(\Omega), \mathbf{u} = \overline{\mathbf{u}} \text{ on } \Gamma_{\mathrm{u}}\}$$
$$V := \{\delta\mathbf{u} : \delta\mathbf{u} \in H^1(\Omega), \delta\mathbf{u} = \mathbf{0} \text{ on } \Gamma_{\mathrm{u}}\}$$

where $H^1(\Omega)$ denotes the Sobolev space of order one. Since, only nodal variable pressure is required, let p and δp be the trial and the test functions for the pressure variable, respectively. Such that $p \in P$ and $\delta p \in P$, we define P by

$$P := \{p : p \in L^2(\Omega), \int_\Omega p \; d\Omega = 0\}$$

where $L^2(\Omega)$ denotes the Sobolev space of order zero. The $u-p$ mixed weak form is given by

$$2\mu \int_\Omega \nabla \mathbf{u} : \nabla \delta \mathbf{u} \; d\Omega - \int_\Omega p \nabla . \delta \mathbf{u} \; d\Omega = \int_\Omega \mathbf{b} . \delta \mathbf{u} \; d\Omega + \int_{\Gamma_t} \bar{\mathbf{t}} . \delta \mathbf{u} \; d\Gamma \qquad \forall \delta \mathbf{u} \in V \tag{7a}$$

$$\int_\Omega \delta p \; (\nabla . \mathbf{u} + \frac{p}{\lambda}) \; d\Omega = 0 \qquad \forall \delta p \in P \tag{7b}$$

The discretization of the weak form leads to a system of linear equations. In the standard $u-p$ mixed formulation both the displacement and the pressure are independent nodal variables. The pressure and the displacement field in Equation (7) is discretized using

$$p_h(\mathbf{x}) = \sum_{I=1}^{N^s} \phi_I(\mathbf{x}) p_I \tag{8a}$$

$$\delta p_h(\mathbf{x}) = \sum_{I=1}^{N^s} \phi_I(\mathbf{x}) \delta p_I \tag{8b}$$

$$u_h(\mathbf{x}) = \sum_{I=1}^{N^+} \phi_I(\mathbf{x}) u_I \tag{9a}$$

$$\delta u_h(\mathbf{x}) = \sum_{I=1}^{N^+} \phi_I(\mathbf{x}) \delta u_I \tag{9b}$$

where p is the nodal pressure, $\mathbf{u}$ is the nodal displacement and ϕ_I are the associated basis functions. In order to ensure the stability of the method, the displacement field is enhanced with bubble basis functions by adding an additional bubble node (denoted by N^b) at the geometric center of each element as shown in Figure 1. The resulting enhanced node set is denoted by N^+ and the standard node set is denoted by N^s, such that $N^+ = N^s \cup N^b$. From Equations (8)-(9), we can observe that the pressure field is approximated over the standard node set N^s, whereas, the displacement field is approximated over the enhanced node set N^+.

In this paper, we discretize the domain with arbitrary polygons and polyhedra in two and three dimensions, respectively. While there are different ways to represent the basis functions over arbitrary polytopes [2], we choose the Wachspress interpolants to describe the unknown fields [39]. These functions are rational polynomials and the construction of the Wachspress basis function is given as: Let $P \subset \mathbb{R}^3$ be a simple convex polyhedron with facets F and vertices V as shown in Figure 2. For each facet $f \in F$, let $\mathbf{n}_f$ be the unit outward normal and for any $\mathbf{x} \in P$, let $h_f(\mathbf{x})$ denote the perpendicular distance of $\mathbf{x}$ to f, which is given by

$$h_f(\mathbf{x}) = (\mathbf{v} - \mathbf{x}) \cdot \mathbf{n}_f \tag{10}$$

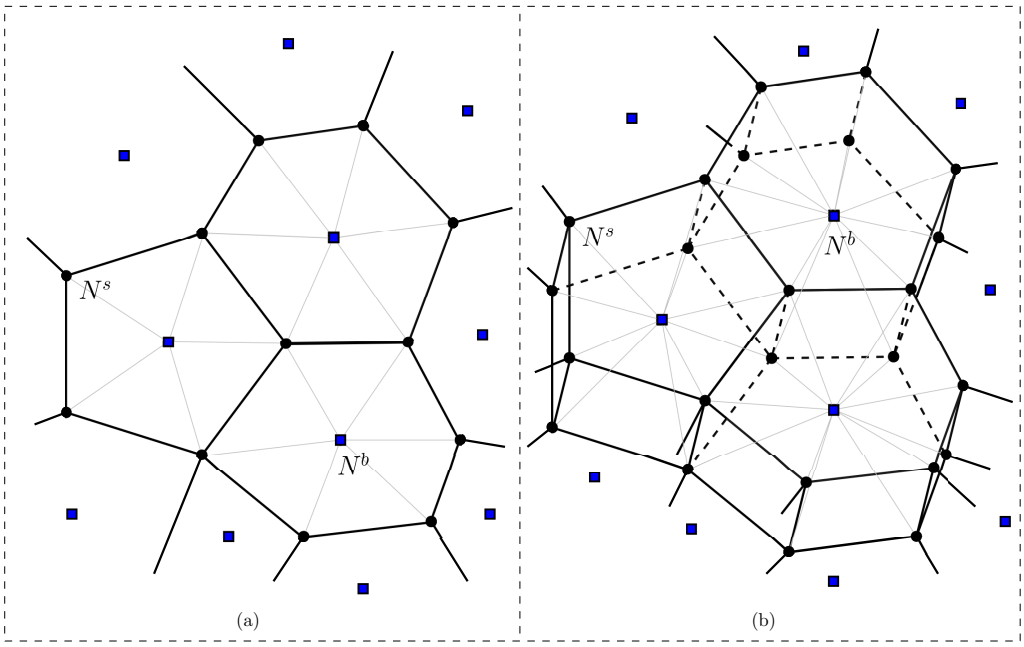

Figure 1: Schematic representation of enhanced node set N^+ for both the two dimensional and three dimensional formulation, respectively. The bubble node set N^b is shown by the filled square inside the element, located at the geometric center of each arbitrary polytope.

for any vertex $\mathbf{v} \in V$ that belongs to f. For each vertex $\mathbf{v} \in V$, let f_1, f_2, f_3 be the three faces incident to $\mathbf{v}$ and for $\mathbf{x} \in P$, let

$$w_{\mathbf{v}}(\mathbf{x}) = \det(\mathbf{p}_{f_1}, \mathbf{p}_{f_2}, \mathbf{p}_{f_3}) \tag{11}$$

where, $\mathbf{p}_f := \mathbf{n}_f / h_f(\mathbf{x})$ is the scaled normal vector, $f_1, f_2, \cdots, f_d$ are the d faces adjacent to $\mathbf{v}$ listed in an counter-clockwise ordering around $\mathbf{v}$ as seen from outside P (see Figure 2) and *det* denotes the regular vector determinant in $\mathbb{R}^d$. The shape functions for $\mathbf{x} \in P$ is then given by

$$\phi_{\mathbf{v}}(\mathbf{x}) = \frac{w_{\mathbf{v}}(\mathbf{x})}{\sum\limits_{\mathbf{u} \in V} w_{\mathbf{u}}(\mathbf{x})}. \tag{12}$$

The Wachspress basis functions are the lowest order shape functions that satisfy boundedness, Kronecker delta property, linearity and linear consistency over arbitrary convex polytopes as shown in Figure 3. The bubble basis functions denoted by ϕ_b are zero along the boundaries of the element and at the standard nodes N^s and one at the bubble node N^b of the element as shown in Figure 3. Mathematically, the bubble basis functions is given by;

$$\phi_{b_e} = (N_e^s)^2 \prod_{I=1}^{N_e^s} \phi_I \tag{13}$$

where, N_e^s, ϕ_{b_e} are the standard node set and bubble node of an element Ω_e as shown in Figure 3.

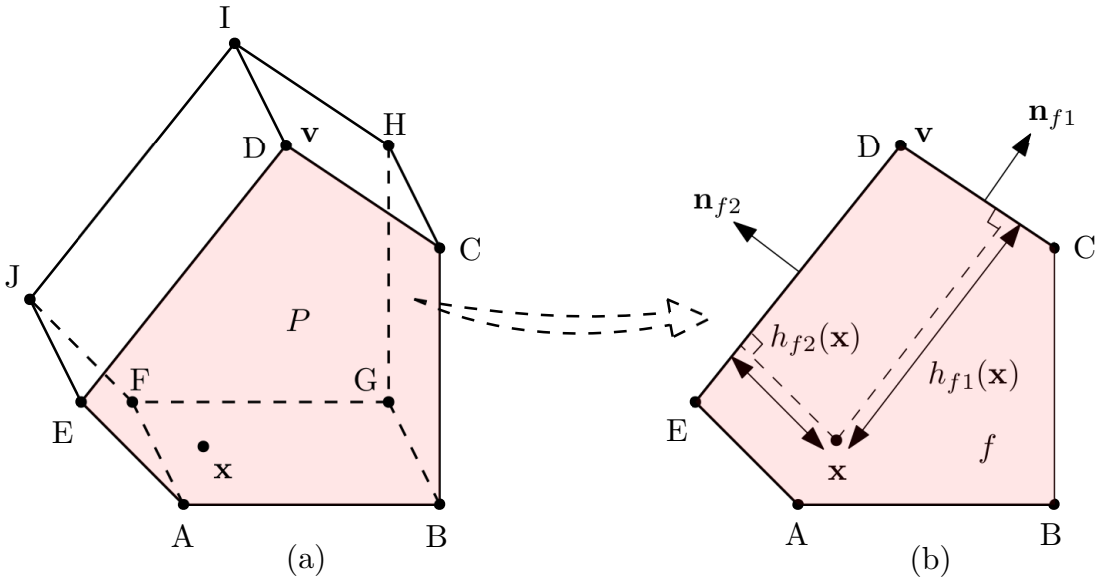

Figure 2: Construction for the Wachspress basis function.

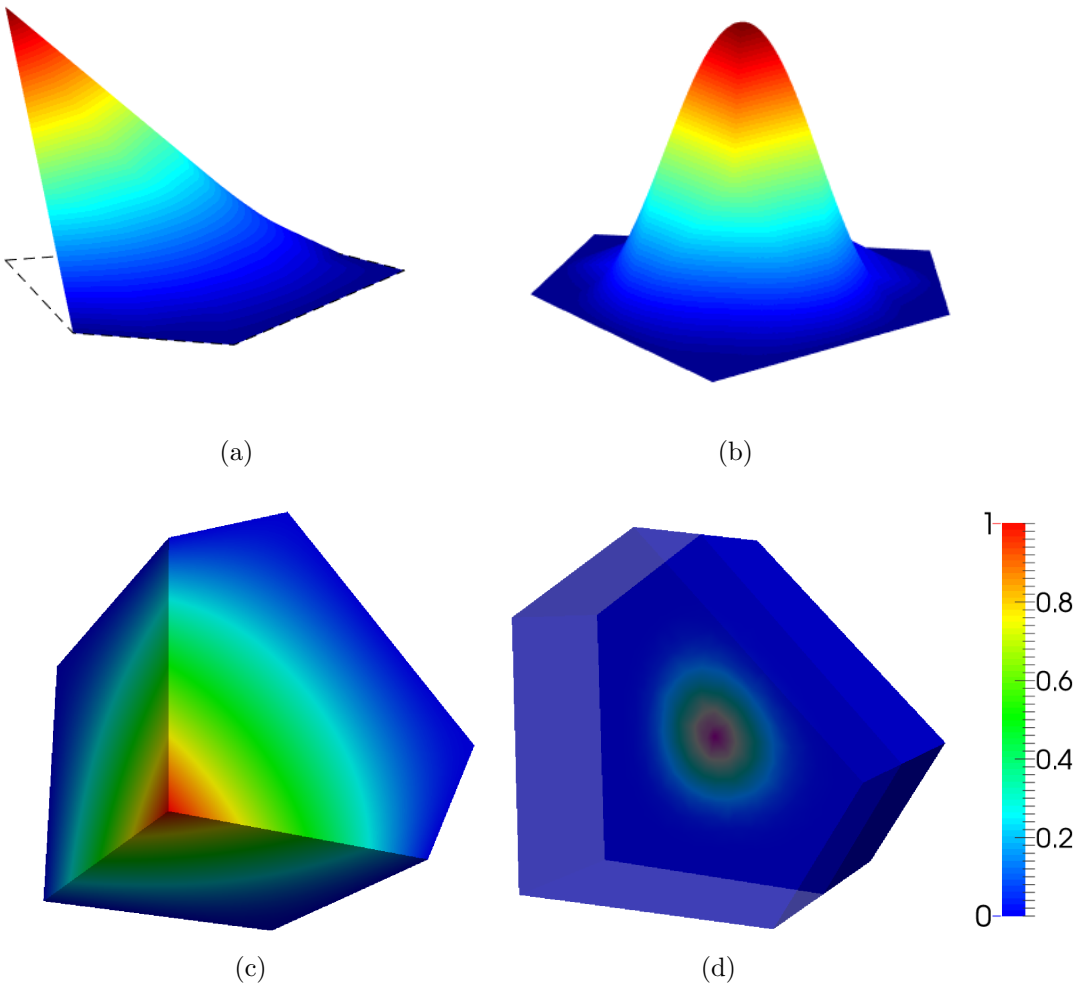

Figure 3: Wachspress basis function: (a) standard node of a pentagon, (b) enhanced/bubble node of a pentagon, (c) standard node of a polyhedra and (d) bubble node of a polyhedra.

2.3. Volume-average nodal projection (VANP) operator

The VANP method inspired by the B-bar method [40], was introduced by Ortiz *et al.,* [32–34] to alleviate volumetric locking for nearly incompressible media in the meshfree methods. The key advantage of the proposed method is that the displacement field and the pressure field are coupled. Such that, the classical $u-p$ mixed formulation can be translated into a purely displacement based formulation using the VANP method. Such that, the classical $u-p$ mixed formulation can be translated into a purely displacement based formulation using the VANP method, which was originally proposed in the finite element pressure projection [37] and RKPM meshfree pressure projection [38] for nearly incompressible hyperelasticity. This implies that the displacement field is the only nodal solution and the pressure field is obtained as post processing.

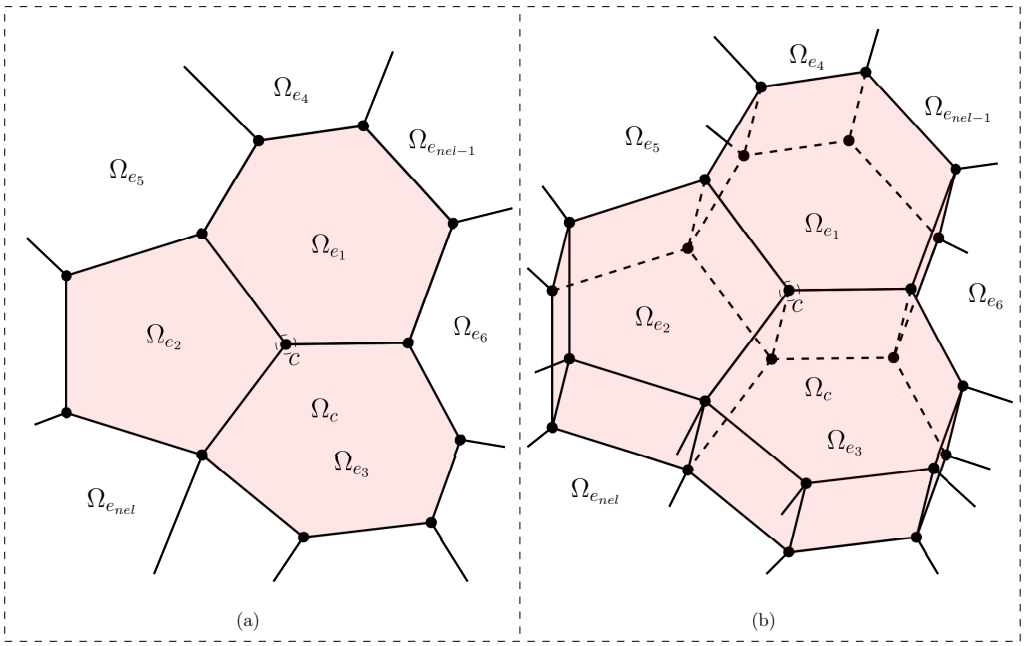

Figure 4: Schematic representation of two and three dimensional integration cell Ω_c, used for the computation of the VANP operator over a current node 'c'.

In this technique, for each current node 'c' of an element (n-sided polygon or polyhedron) an integration cell denoted by Ω_c is created, as shown in Figure 4. All the elements attached to the current node 'c' becomes the part of the integration cell Ω_c as shown in Figure 4. The integration cell Ω_c created is used to evaluate the projection operator denoted by π, which is later used to calculate the modified strain denoted by $\overline{\boldsymbol{\varepsilon}}_h(\mathbf{u}_h)$ to alleviate locking phenomenon. In this process, an additive decomposition is applied to the standard total strain, which leads to:

$$\begin{aligned}\boldsymbol{\varepsilon}_h(\mathbf{u}_h) &= \boldsymbol{\varepsilon}_h^{dev}(\mathbf{u}_h) + \boldsymbol{\varepsilon}_h^{vol}(\mathbf{u}_h) \\ &= \left(\boldsymbol{\varepsilon}_h(\mathbf{u}_h) - \frac{1}{3}\text{tr }\boldsymbol{\varepsilon}_h(\mathbf{u}_h)\mathbf{I}\right) + \frac{1}{3}\text{tr }\boldsymbol{\varepsilon}_h(\mathbf{u}_h)\mathbf{I}\end{aligned} \tag{14}$$

In the present method, the dilatational part is projected onto the another space which helps to alleviate the volumetric locking. The projection operator denoted by π operates over the

dilatational strain $\boldsymbol{\varepsilon}_h^{vol}(\mathbf{u}_h)$. Thus, the projected dilatational strain is denoted by $\overline{\boldsymbol{\varepsilon}}_h^{vol}(\mathbf{u}_h)$. The total modified strain is called as a discrete modified strain denoted by $\overline{\boldsymbol{\varepsilon}}_h(\mathbf{u}_h)$ is evaluated as:

$$\overline{\boldsymbol{\varepsilon}}_h(\mathbf{u}_h) = \boldsymbol{\varepsilon}_h^{dev}(\mathbf{u}_h) + \pi\left[\boldsymbol{\varepsilon}_h^{vol}(\mathbf{u}_h)\right] = \boldsymbol{\varepsilon}_h^{dev}(\mathbf{u}_h) + \overline{\boldsymbol{\varepsilon}}_h^{vol}(\mathbf{u}_h) \tag{15}$$

The pressure constraint is obtained by substituting Equations (8)-(9) into Equation (7b). It can be shown that after relying on the arbitrariness of the nodal pressure test functions the discrete pressure term leads to the following:

$$\int_\Omega \sum_{I=1}^{N^s} \phi_I(\mathbf{x})\delta p_I \left\{\nabla.\mathbf{u}_h + \frac{1}{\lambda}\sum_{I=1}^{N^s}\phi_I(\mathbf{x})p_I\right\} d\Omega = 0 \qquad \forall \delta p \in P \tag{16a}$$

$$\int_\Omega \phi_I(\mathbf{x})\nabla.\mathbf{u}_h \; d\Omega + \frac{1}{\lambda}\sum_{I=1}^{N^s}\int_\Omega \phi_I(\mathbf{x})\phi_I(\mathbf{x})p_I \; d\Omega = 0 \tag{16b}$$

The above integration is performed over an integration cell Ω_c to evaluate pressure field at any node for example say node 'c' (see Figure 4) is given by

$$\begin{aligned} p_c(\mathbf{x}) &= -\lambda \sum_{I=1}^{N^s} \phi_I(\mathbf{x}) \frac{\int_{\Omega_c} \phi_c(\mathbf{x})\nabla.\mathbf{u}_h \; d\Omega}{\int_{\Omega_c} \phi_c(\mathbf{x}) \; d\Omega} \\ &= -\lambda \sum_{I=1}^{N^s} \phi_I(\mathbf{x}) \frac{\int_{\Omega_c} \phi_c(\mathbf{x})\boldsymbol{\varepsilon}_h^{vol} \; d\Omega}{\int_{\Omega_c} \phi_c(\mathbf{x}) \; d\Omega} \end{aligned} \tag{16c}$$

which is called the *volume-averaged nodal pressure*. The nodal pressure is evaluated as post processing using only the standard node set N^s. From Equation (16c), the bar operator (π_c) is given by

$$\pi_c[.] = \frac{\int_{\Omega_c} \phi_c(\mathbf{x})[.] \; d\Omega}{\int_{\Omega_c} \phi_c(\mathbf{x}) \; d\Omega} \tag{17}$$

The VANP operator denoted $\pi[.]$ is evaluated by the linear combination over the bar operator given as:

$$\pi[.] = \sum_{I=1}^{N^s} \phi_I(\mathbf{x})\pi_c[.] \tag{18}$$

Thus, the projected dilatational strain $\overline{\boldsymbol{\epsilon}}_h^{vol}$ is computed as follows:

$$\overline{\boldsymbol{\varepsilon}}_h^{vol} = \pi[\boldsymbol{\varepsilon}_h^{vol}] = \sum_{I=1}^{N^s} \phi_I(\mathbf{x})\pi_c[\boldsymbol{\varepsilon}_h^{vol}] = \sum_{I=1}^{N^s} \phi_I(\mathbf{x}) \left\{\frac{\int_{\Omega_c} \phi_c(\mathbf{x})\boldsymbol{\varepsilon}_h^{vol} \; d\Omega}{\int_{\Omega_c} \phi_c(\mathbf{x}) \; d\Omega}\right\} \tag{19}$$

2.4. Discrete equations

The domain Ω is partitioned into n_{el} non-overlapping polygonal elements with straight edges and polyhedral elements with planar/non-planar faces in two dimensions and three dimensions, respectively. The proposed method is purely the displacement based method as the pressure field is derived in terms of the volumetric strain. In order to ensure stability of the solution, the displacement field is computed over the enhanced node set N^+. As in finite element the discrete strain relation is given by:

$$\boldsymbol{\varepsilon}_h(\mathbf{u}_h) = \sum_{I=1}^{N^+} \mathbf{B}_{\mathrm{I}}(\mathbf{x})\mathbf{u}_{\mathrm{I}} \tag{20a}$$

$$\boldsymbol{\varepsilon}_h(\delta\mathbf{u}_h) = \sum_{I=1}^{N^+} \mathbf{B}_{\mathrm{I}}(\mathbf{x})\mathbf{u}_{\mathrm{I}} \tag{20b}$$

$$\overline{\boldsymbol{\varepsilon}}_h^{vol}(\mathbf{u}_h) = \sum_{I=1}^{N^s} \phi_I(\mathbf{x})\pi_c \left[\mathbf{m}^{\mathrm{T}} \sum_{I=1}^{N^+} \mathbf{B}_{\mathrm{I}}\right] \mathbf{u}_I \tag{20c}$$

$$\overline{\boldsymbol{\varepsilon}}_h^{vol}(\delta\mathbf{u}_h) = \sum_{I=1}^{N^s} \phi_I(\mathbf{x})\pi_c \left[\mathbf{m}^{\mathrm{T}} \sum_{I=1}^{N^+} \mathbf{B}_{\mathrm{I}}\right] \delta\mathbf{u}_I \tag{20d}$$

where $\mathbf{m}$ is the linear operator and $\mathbf{B}_I(\mathbf{x})$ is the strain displacement matrix for enhanced node N^+, given by:

$$\mathbf{m} = [1\ 1\ 0]^{\mathrm{T}} \tag{21a}$$

$$\mathbf{B}_I = \begin{bmatrix} \phi_{I,x} & 0 \\ 0 & \phi_{I,y} \\ \phi_{I,y} & \phi_{I,x} \end{bmatrix} \tag{21b}$$

for two dimensions and in three dimensions

$$\mathbf{m} = [1\ 1\ 1\ 0\ 0\ 0]^{\mathrm{T}} \tag{22a}$$

$$\mathbf{B}_I = \begin{bmatrix} \phi_{I,x} & 0 & 0 \\ 0 & \phi_{I,y} & 0 \\ 0 & 0 & \phi_{I,z} \\ \phi_{I,y} & \phi_{I,x} & 0 \\ \phi_{I,z} & 0 & \phi_{I,x} \\ 0 & \phi_{I,z} & \phi_{I,y} \end{bmatrix} \tag{22b}$$

where $\phi_{I,j}(j = x, y, z)$ is the derivative of shape functions. The above strain is computed over the displacement degrees of freedom i.e. over the enhanced node set. These discrete quantities are substituted into weak form which leads to the following system of equations:

$$\left(\mathbf{K}^{dev} + \mathbf{K}^{vol}\right)\mathbf{u} = \mathbf{f} \tag{23}$$

where $\mathbf{u}$ is the column vector of nodal coefficients. The external force vector, $\mathbf{f}$ and the stiffness matrix are given by:

$$\mathbf{K}^{dev} = \int_{\Omega} \mathbf{B}^{\mathrm{T}} \mathbf{C}_{\mu} \mathbf{B} \; d\Omega \tag{24a}$$

$$\mathbf{K}^{vol} = \lambda \int_{\Omega} \mathbf{B}^{\mathrm{T}} \mathbf{m} \sum_{I=1}^{N^s} \phi_I \pi_c \left[\mathbf{m}^{\mathrm{T}} \mathbf{B} \right] \; d\Omega \tag{24b}$$

$$\mathbf{f} = \int_{\Omega} \phi_I \mathbf{b} \; d\Omega + \int_{\Gamma_t} \phi_I \bar{\mathbf{t}} \; d\Gamma \tag{24c}$$

and the constitutive matrix is given by:

$$\mathbf{C}_{\mu} = \begin{bmatrix} 2\mu & 0 & 0 \\ 0 & 2\mu & 0 \\ 0 & 0 & \mu \end{bmatrix} \tag{25}$$

in two dimensions, and

$$\mathbf{C}_{\mu} = \begin{bmatrix} 2\mu & 0 & 0 & 0 & 0 & 0 \\ 0 & 2\mu & 0 & 0 & 0 & 0 \\ 0 & 0 & 2\mu & 0 & 0 & 0 \\ 0 & 0 & 0 & \mu & 0 & 0 \\ 0 & 0 & 0 & 0 & \mu & 0 \\ 0 & 0 & 0 & 0 & 0 & \mu \end{bmatrix} \tag{26}$$

in three dimensions. The nodal coefficients i.e. nodal displacements are obtained by solving Equation (23).

3. Constant smoothing

In this paper, the constant smoothing method is used for computing the terms in Equation (23). For the purpose of numerical integration, the elements are divided into subcells denoted by Ω_s as shown in Figure 5. In this study, we use triangular subcells in the two dimensional space and tetrahedral subcells in the three dimensional space as shown in Figure 5. The strain smoothing technique is then applied within each subcell to evaluate the modified strain. For simplicity of the notation, the derivation of the smoothing scheme is given in detail only for the two-dimensions. The Cartesian coordinate system is chosen, where for convenience $x \equiv x_1$ and $y \equiv x_2$. In addition, n_j $(j = 1, 2)$ is the j-th component of the unit outward normal to a cell edge in the Cartesian coordinate system. The discrete strain field $\tilde{\varepsilon}_{ij}^h$ that yields the modified strain-displacement matrix $\tilde{\mathbf{B}}$ that is used to build the stiffness matrix is computed by a weighted average of the standard strain field ε_{ij}^h in each subcell Ω_s^h, as follows:

$$\tilde{\varepsilon}_{ij}^h = \int_{\Omega_s^h} \varepsilon_{ij}^h(\mathbf{x}) f(\mathbf{x}) d\Omega, \tag{27}$$

where $f(\mathbf{x})$ is a smoothing function. On writing Equation (27) at the basis functions derivatives level, its right-hand side can be expressed in terms of the divergence theorem, as follows:

$$\int_{\Omega_s^h} \phi_{I,j} f(\mathbf{x})\, d\Omega = \int_{\Gamma_s^h} \phi_I f(\mathbf{x}) n_j\, d\Gamma - \int_{\Omega_s^h} \phi_I f_{,j}(\mathbf{x})\, d\Omega. \tag{28}$$

where Ω_s is the domain of the smoothing cell bounded by Γ_s and n_j are the outward normals. The ϕ_I are the Wachspress shape functions at the cartesian coordinates and $\phi_{I,j}$ are the modified derivative to be evaluated for the element. The above Equation (28) was coined as *divergence consistency* in Duan et al. [41], where it was introduced to correct integration errors in second- and third-order meshfree approximations. This divergence consistency was later used to correct integration errors in the meshfree method [42, 43]. The above Equation (28), originated by the so called "integration constraint" in Chen et al. [13] in the form of divergence condition, was coined as *divergence consistency* in Duan et al. [41]. The extension of integration constraint to higher order meshfree approximation has been introduced in [14, 42, 43]. In the constant smoothing method, the smoothing function is chosen to be a constant, that is,

$$f(\mathbf{x}) = 1 \tag{29}$$

The divergence consistency equation reduces to,

$$\int_{\Omega_s^h} \phi_{I,j}\, d\Omega = \int_{\Gamma_s^h} \phi_I n_j\, d\Gamma \tag{30}$$

The above equation is the strain smoothing of the stabilized conforming nodal integration (SCNI) [13] and can be used to obtain the modified derivative, $\phi_{I,j}$. On numerical integration of the above equation over Ω_s. We get,

$$\sum_{m=1}^{mg} W_m \phi_{I,j}(x_m) = \sum_{s=1}^{sl} \sum_{g=1}^{gl} \phi_I(x_g) n_j^L W_g \tag{31}$$

where mg and W_m are number of Gauss points and corresponding weights per smoothing cell, respectively. Only one Gauss point (mg) is required for the numerical integration of the smoothing cell as shown in Figure 5. Following the sub-domain stabilized conforming nodal integration originally proposed in [15], only one Gauss point (mg) is required for the numerical integration of the smoothing cell as shown in Figure 5. Similarly, gl and W_g are Gauss points and corresponding weights along the boundary (edges) of the subcell, respectively. The Gauss points required for the numerical integration along the boundaries of the smoothing cell are: two (i.e. $gl = 2$) for two dimensions and three (i.e. $gl = 3$) for the three dimensions, as shown in Figure 5. While sl represents the number of edges/faces. The modified derivatives of the shape functions thus obtained using cell based smoothing technique are used to compute the strain displacement matrix i.e $\mathbf{B}_I$ as shown in Equations (21) and (22), respectively.

4. Numerical Examples

In this section, we demonstrate the accuracy and the convergence properties of the proposed VANP method with constant smoothing over arbitrary polytopes for nearly-incompressible

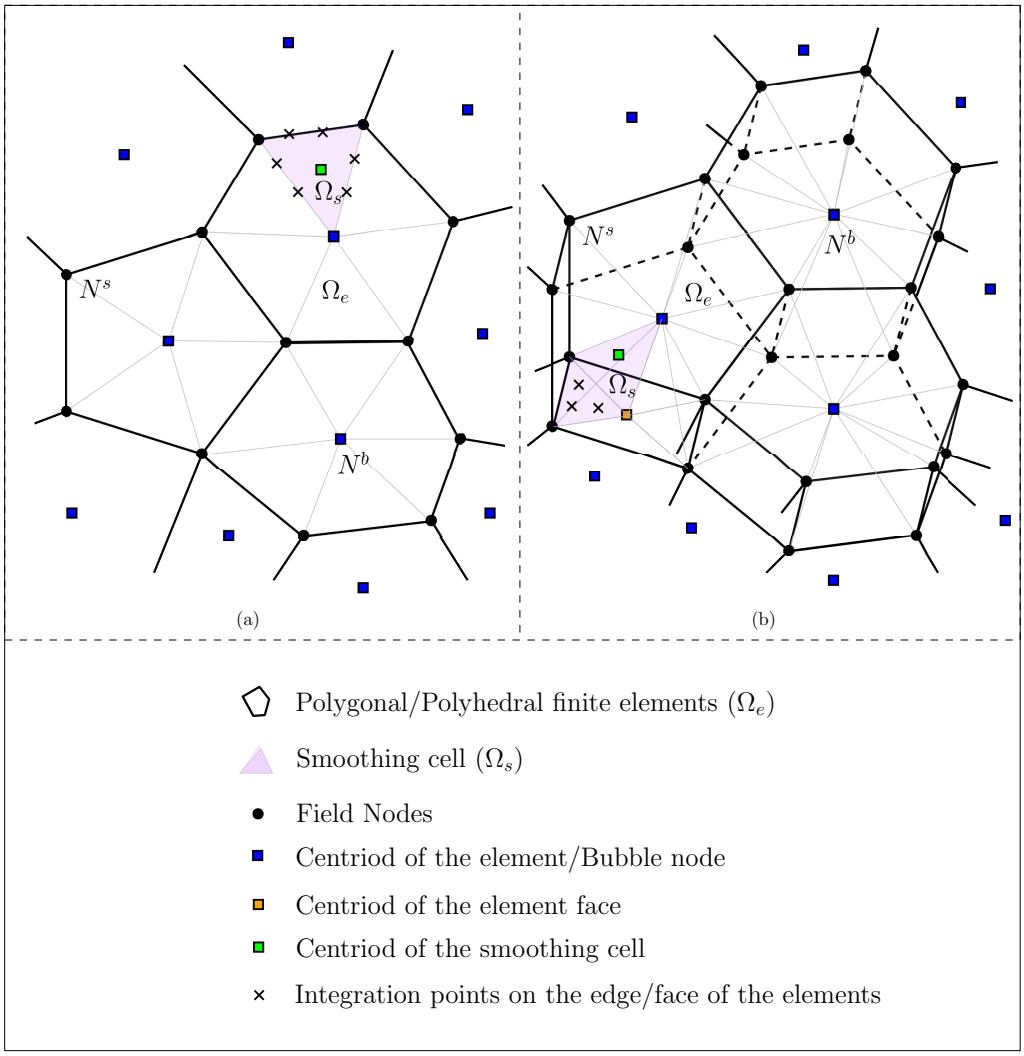

Figure 5: Schematic representation of the integration points within the domain shown by the centroid of the smoothing cell and on the edges/faces of the subcell Ω_s shown by the cross for constant smoothing, where the filled square node (i.e the centroid of the element) is to discretize the element into the smoothing cells.

problems in two and three dimensions. The discretization is based on centroid Voronoi tessellation. The two dimensional region is discretized with polygons using Polymesher [3], a MATLAB based meshing tool. For three dimensional problems, we employ the approach proposed in [19] to generate polyhedral meshes. The results from the proposed method are compared with MINI [44] and analytical solutions where available. The relative error in L^2 norm and H^1 seminorm is used to assess the accuracy and the convergence rates of the proposed framework. Whilst discussing the results, the following convention is adopted:

- VANP-CS- for the proposed VANP method with constant smoothing over arbitrary polytopes.
- VANP- for the VANP method over arbitrary polytopes.
- PFEM- for the conventional polygonal finite element method.

- MINI- for the triangular and tetrahedral finite element.

4.1. Applications to two dimensional problems

We first study the convergence and the accuracy properties of the proposed VANP-CS over arbitrary polytopes in two dimensions. Three problems are considered: (a) patch test, (b) cantilever beam with end shear load and (c) driven cavity flow.

Patch test. In the first example, the convergence and the accuracy properties are demonstrated with a linear patch test and the results are compared with the classical PFEM. For this, consider a unit square, $\Omega \in (0,1)^2$ subjected to the following conditions on the boundary, Γ_u:

$$\begin{pmatrix} u(x,y) \\ v(x,y) \end{pmatrix} = \begin{pmatrix} x \\ x+y \end{pmatrix} \tag{32}$$

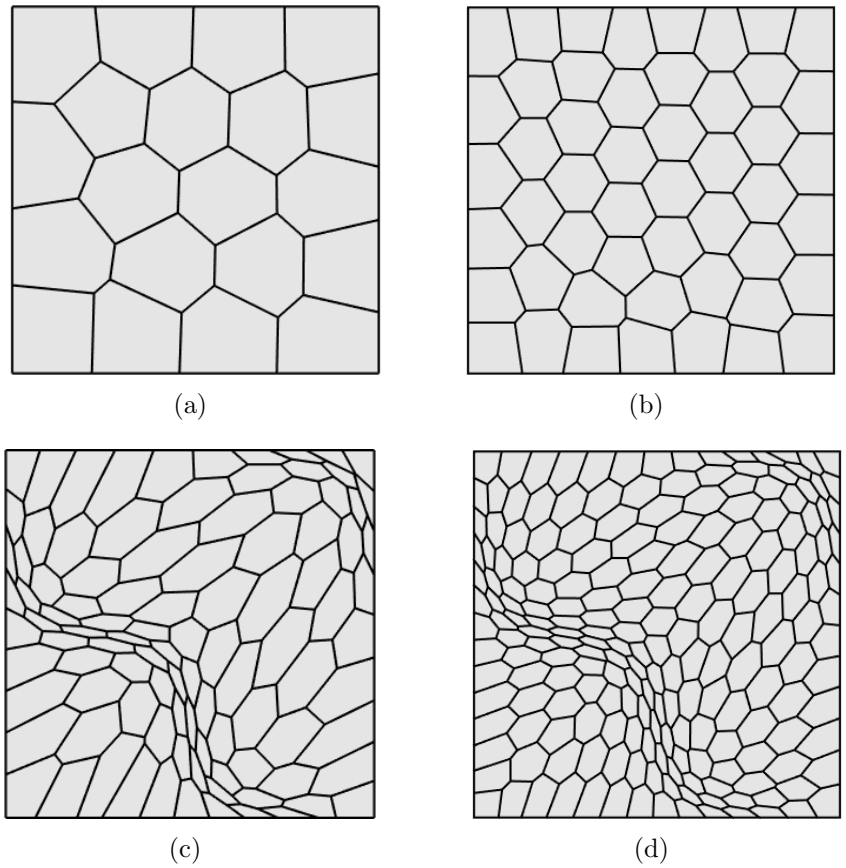

Figure 6: Square domain: the sample meshes showing domain discretization with polygonal element.

Figure 6 shows four different polygonal meshes employed for this study. A state of plane strain condition is assumed with the following material properties: Young's modulus $E = 3\times10^7$ MPa and Poisson's ratio $\nu = 0.499$ [45]. The relative error in the L^2 norm and H^1 seminorm are given in Table 1. It can be inferred from the results that the patch test is satisfied up-to machine precision for the nearly incompressible material behavior with the proposed VANP-CS method over the arbitrary polygons in two dimensions.

Table 1: Relative error in the L^2 norm and H^1 seminorm for the two-dimensional linear patch test.

Mesh	PFEM		VANP-CS	
	L^2	H^1	L^2	H^1
(a)	1.24×10^{-06}	6.20×10^{-06}	4.67×10^{-15}	1.89×10^{-14}
(b)	1.94×10^{-06}	7.26×10^{-06}	1.62×10^{-14}	2.95×10^{-14}
(c)	1.54×10^{-05}	7.71×10^{-05}	2.61×10^{-14}	7.81×10^{-14}
(d)	3.47×10^{-05}	1.10×10^{-04}	2.91×10^{-14}	1.10×10^{-13}

Cantilever beam. In this two dimensional problem, consider a cantilever beam of length $L = 8$ m and height $D = 4$ m, subjected to a parabolic shear load, $P = 250$ N at the free end as shown in Figure 7(a).

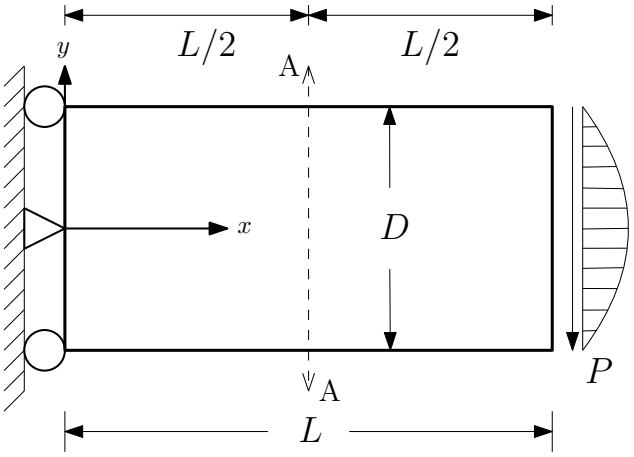

(a)

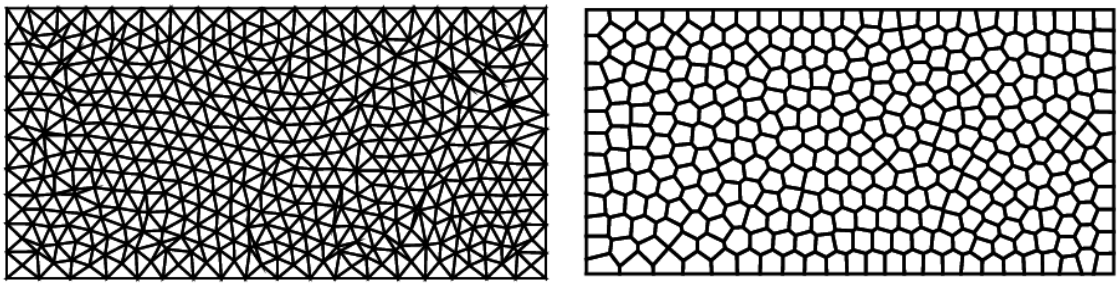

(b) (c)

Figure 7: Cantilever beam: (a) geometry and boundary conditions, (b-c) representative triangular (901 elements) and polygonal mesh (320 elements), respectively.

The exact solution for this problem is given by [46]:

$$u(x,y) = \frac{Py}{6\overline{E}I}\left[(6L-3x)x + (2+\overline{\nu})\left(y^2 - \frac{D^2}{4}\right)\right]$$
$$v(x,y) = -\frac{P}{6\overline{E}I}\left[3\overline{\nu}y^2(L-x) + (4+5\overline{\nu})\frac{D^2x}{4} + (3L-x)x^2\right] \tag{33}$$

where $I = \dfrac{D^3}{12}$ is the moment of inertia, $\overline{E} = E/(1-\nu^2)$, $\overline{\nu} = \nu/(1-\nu)$ for plane strain condition. Figure 7(c) shows a representative polygonal mesh employed in this example. The convergence of the relative error in the L^2 norm and H^1 seminorm with mesh refinement with the proposed framework is shown in Figure 8 and the values are tabulated in Table 2. The influence of different Poisson's ratio ($\nu = 0.3,\ 0.45,\ 0.4999999$) is also shown. It can be inferred that the proposed framework yields accurate results for all values of Poisson's ratio and converges at the optimal convergence rate. It can be further opined that the VANP-CS suppresses the volumetric locking.

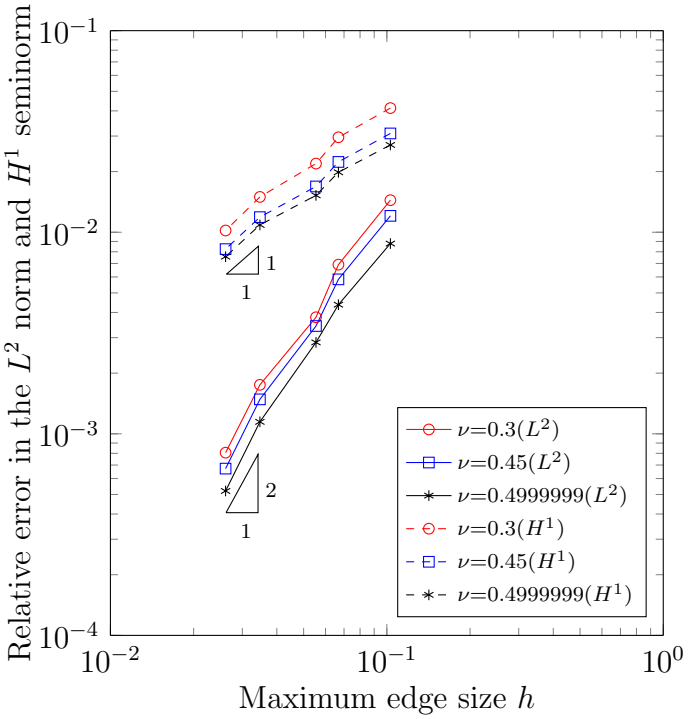

Figure 8: Cantilever beam: Convergence rate for the L^2 norm and H^1 seminorm using polygonal element is optimal and accurate with VANP-CS for different Poisson's ratio i.e for both the compressible and nearly-incompressible problem.

Next, the convergence and the accuracy of the proposed VANP-CS is demonstrated by comparing the results with conventional PFEM[2] and with MINI element. For comparison

[2]without nodal projection (i.e. PFEM) and without strain smoothing (i.e., VANP) to compute the terms in the bilinear/lienar form

Table 2: The convergence of the VANP-CS method with mesh refinement for different Poisson's ratio.

Element size	L^2 norm			H^1 seminorm		
h	$\nu = 0.3$	$\nu = 0.45$	$\nu = 0.4999999$	$\nu = 0.3$	$\nu = 0.45$	$\nu = 0.4999999$
0.1030	0.0144	0.0120	0.0087	0.0412	0.0309	0.0270
0.0668	0.0069	0.0058	0.0043	0.0295	0.0223	0.0198
0.0554	0.0037	0.0034	0.0028	0.0219	0.0168	0.0152
0.0347	0.0017	0.0014	0.0011	0.0149	0.0118	0.0108
0.0261	0.0008	0.0006	0.0005	0.0101	0.0082	0.0075

with the MINI element, the domain is discretized with triangular elements (see Figure 7(b) for a representative mesh). Figure 9(a) shows the relative error in the L^2 norm as a function of Poisson's ratio for different approaches for a mesh of 160 polygonal elements and 217 triangular elements. For comparison, the dofs are kept almost the same for comparison. It is clear that the conventional PFEM suffers from volumetric locking in the near incompressibility limit, whilst all other approaches are free from locking. Note that VANP over polygons and VANP-CS both alleviate locking syndrome, however, VANP over polygons requires 'many' integration points to compute the bilinear and linear form. The strain smoothing on the other hand, reduces the computational burden. The convergenece of the relative error in the L^2 norm and H^1 seminorm with mesh refinement for different approaches for the Poisson's ratio $\nu = 0.4999999$ is shown in Figure 9. It can be opined that the proposed framework VANP with and without strain smoothing alleviates volumetric locking, yields accurate results and converges at optimal convergence rate. Figure 10 shows the pressure contour for the cantilever beam when meshed with triangular and poylgonal elements. From Figures 10(a)-10(b), it can be seen that the nodal pressure solution does not show any osciallation. Figure 10(c) shows the pressure profile through the thickness of the beam at $x = 4$ for conventional PFEM, MINI and VANP-CS. The conventional PFEM shows pressure oscillations, whilst MINI and VANP-CS does not show any pressure oscillations for same degrees of freedom, as expected. Moreover, we can observe that the performance of coarser polygonal meshes is similar to the performance of the simplest finite element (i.e. triangular elements).

Poiseuille flow problem. Next, we consider Poiseuille flow problem. For this example, we consider a two dimensional unit square domain under plane strain condition with a nearly incompressible limit. Figure 11(a) shows the geometry and the boundary conditions employed in this study. The analytical solution for the displacement and the pressure is given by:

$$u = 4y(1-y); \quad v = 0; \qquad P = 8(1-x). \tag{34}$$

The analytical displacements are prescribed on the boundary of the domain and the left bottom corner is subjected to zero pressure condition (see Figure 11(a). A representative polygonal mesh used is shown in Figure 11(b). Figure 12 shows the convergence of the relative error in the displacement and the pressure with mesh refinement. It can be inferred that the method yields accurate results and converges at optimal convergence rate in both the displacement and pressure. Figure 13 shows the displacement contours along the x direction and displacement profile along the section B-B. It is seen that the proposed method is accurate even on a coarser grid.

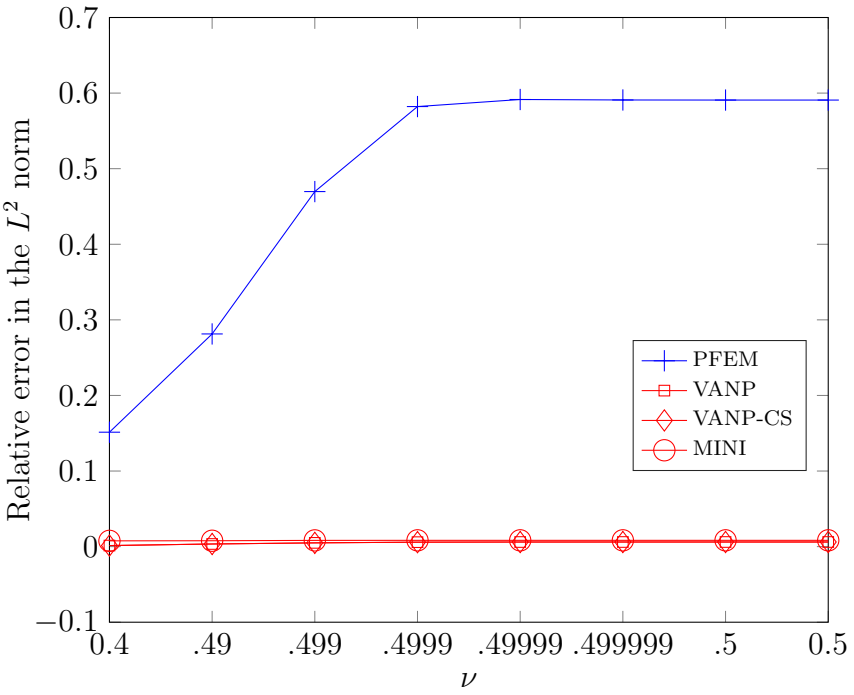

(a)

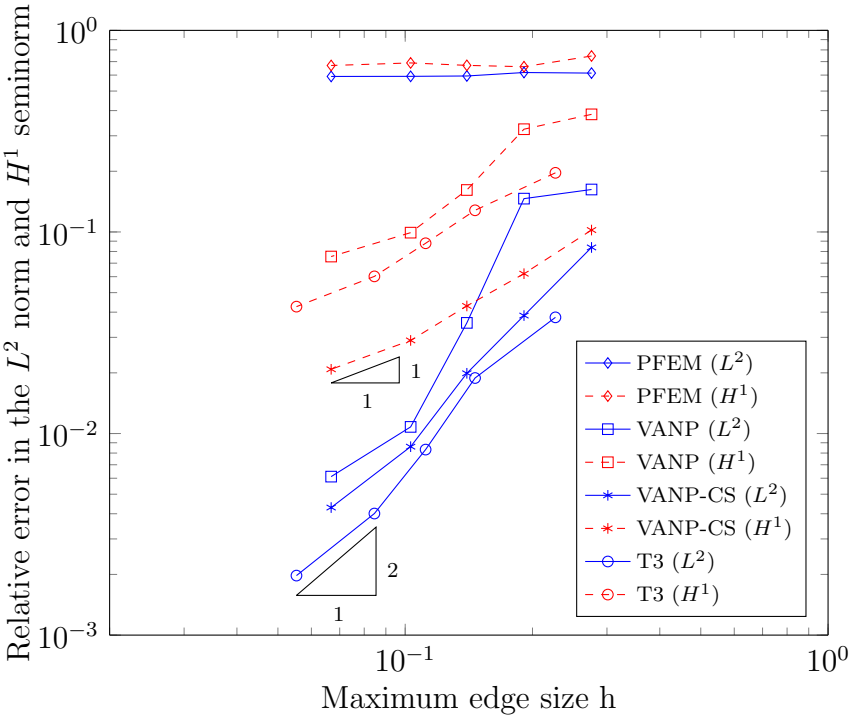

(b)

Figure 9: Cantilever beam: (a) Relative error in the L^2 norm for different Poisson's ratio using polygonal elements (PFEM, VANP, VANP-CS) (160 polygonal elements with 638 degrees of freedom) and triangular elements (MINI) (217 triangular elements with 678 degrees of freedom). (b) Convergence rate for the relative error in L^2 norm and H^1 seminorm for $\nu = 0.4999999$ using different methods.

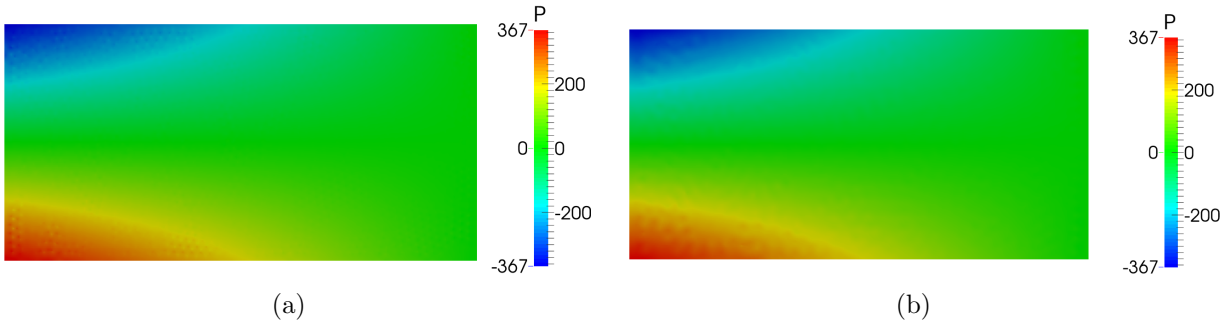

(a) (b)

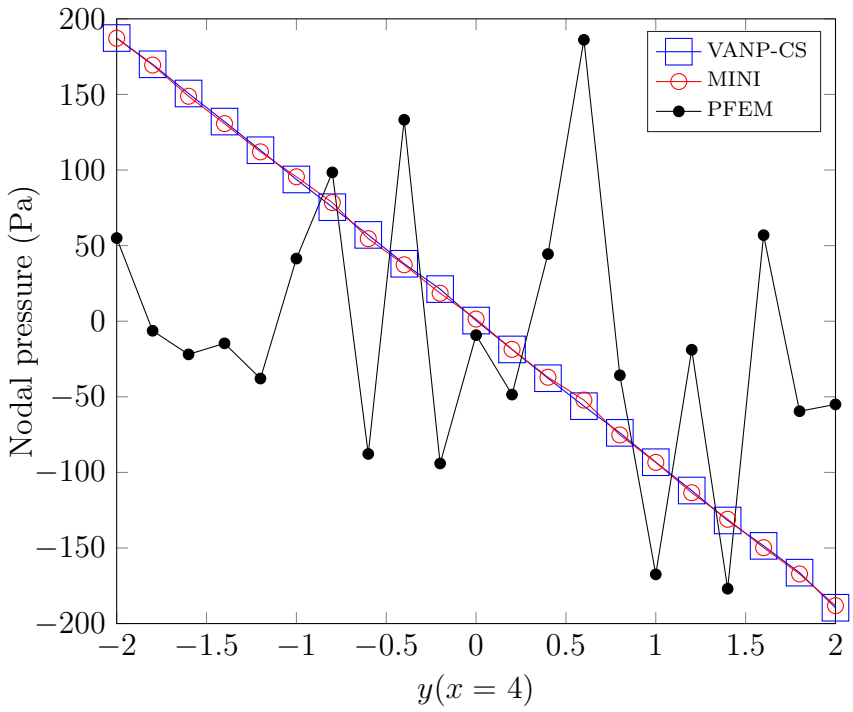

(c)

Figure 10: Cantilever beam discretized with triangular and polygonal elements with 11274 degrees of freedom for both the elements: (a) nodal pressure for 1890 polygonal elements (b) nodal pressure for 3724 triangular elements (c) nodal pressure (Pa) values along a section at $x = 4$m using VANP and MINI over the given discretization.

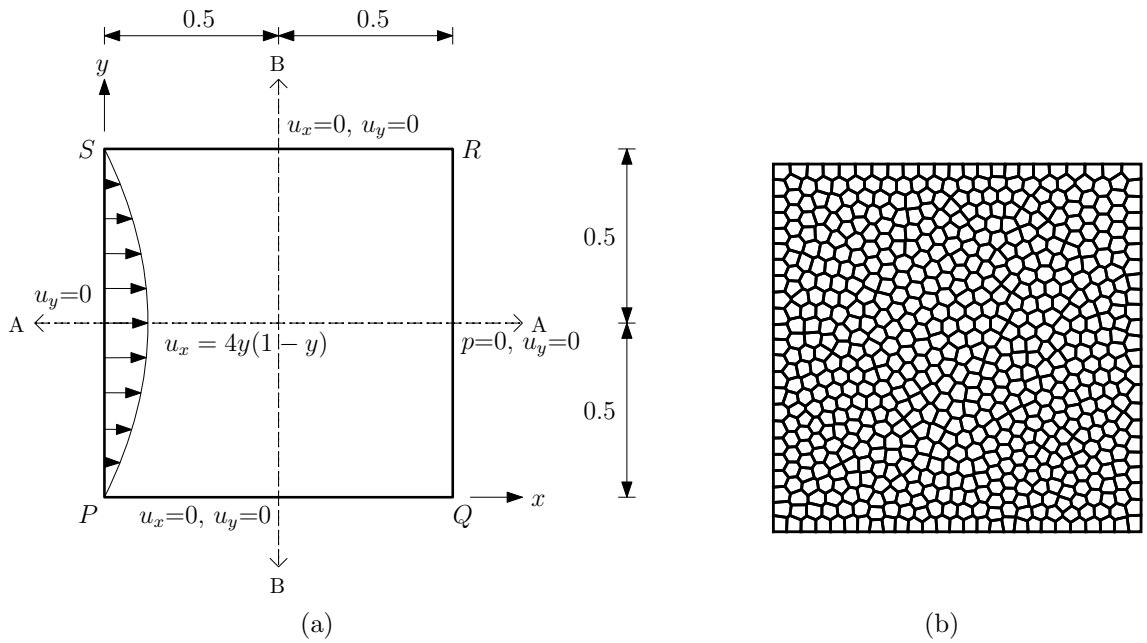

Figure 11: Poiseuille flow:(a) Geometry and boundary condition (b) representative mesh of 640 polygonal elements.

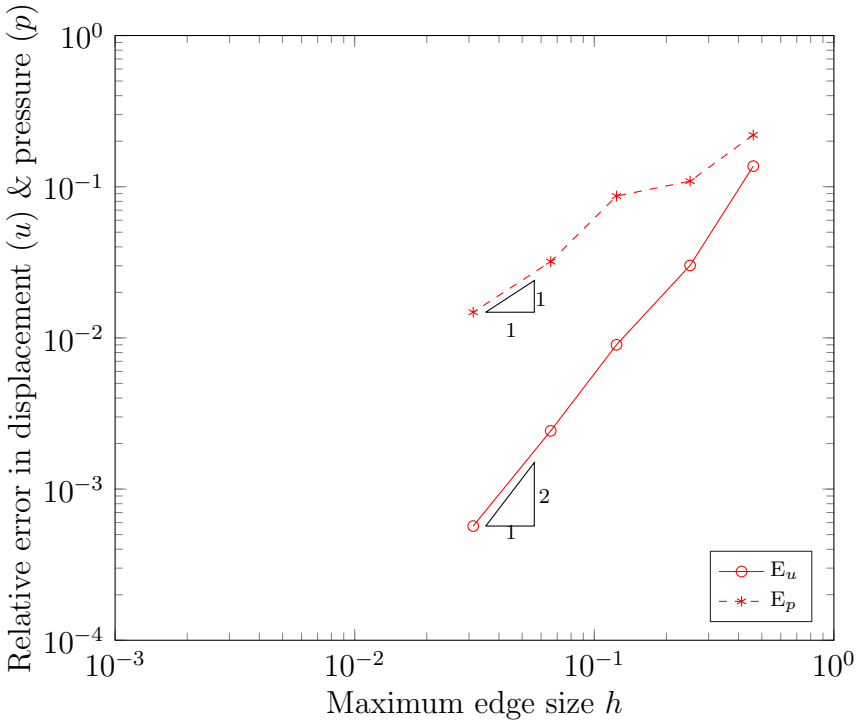

Figure 12: Poiseuille flow: Relative error in the displacement (u) and pressure (p) converges well with the mesh refinement with an optimal convergence rate for ν=0.4999999.

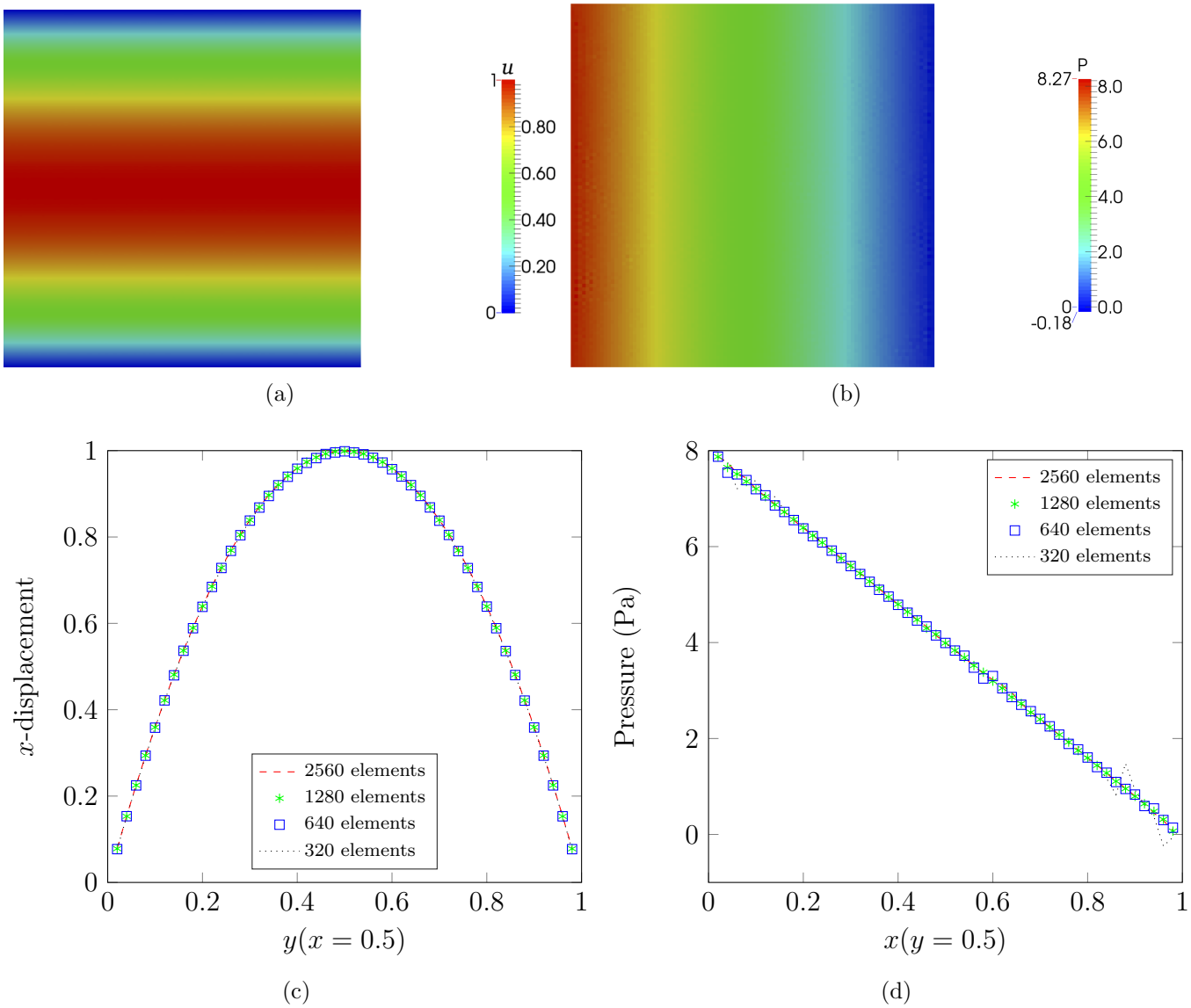

Figure 13: Poiseuille flow: (a) Displacement in x direction contour plot, (b) Nodal pressure (Pa) profile using polygonal elements, (c) Displacement in x direction along section B-B, for different polygonal discretization and (d) Pressure along section A-A, for different polygonal discretization.

The pressure profile for this problem is shown in Figure 13(b) for the finest mesh. This shows the stability of pressure within the domain for nearly incompressibility limit of $\nu = 0.4999999$. The stability in the pressure is also examined by evaluating pressure at section A-A for different mesh discretization, see Figure 11(a). Figure 13(d) illustrates the stability in the pressure with mesh refinement along a section A-A. Further, the numerical inf-sup value evaluated with mesh refinement is presented in Table 3, where, $\gamma_h = \sqrt{\lambda_k}$ and λ_k is the smallest non-zero eigenvalue. The details of the numerical inf-sup can be found in [47]. It can be inferred from Table 3 that the numerical inf-sup test value converges to a value that is bounded away from zero with mesh refinement. Therefore, the VANP method passes the numerical inf-sup test and is stable.

Table 3: Values of γ_h in the numerical inf-sup tests. The domain is discretized with arbitrary polytopes

Number of elements	h	γ_h
40	0.25	0.4087
80	0.18	0.4214
160	0.12	0.4192
320	0.08	0.4222

4.2. Applications to three dimensional problems

Next, we study the convergence properties of the proposed framework over star convex polytopes in three dimensions. Two problems are considered: (a) Cook's membrane problem and (b) the short cantilever problem. As both these problems do not have analytical solutions, an overkill finite element solution is used as a reference solution. The finite element solution is computed using the commercial software Abaqus, with the domain discretized with tetrahedral elements (C3D10H) or hexahedral elements (C3D8H).

Cook's membrane. Consider the standard bending dominated Cook's membrane. The geometry and the boundary conditions are shown in Figure 14(a). The right end of the membrane is subjected to an in-plane shear load, $P = 1$ N and the left end is fixed in all the three directions, resulting in a deformation that is dominated by bending. A sample mesh used in the study is shown in Figure 14(b). The material properties are: Young's modulus $E = 1$ Pa and Poisson ratio $\nu = 0.4999999$. The reference solution is obtained with a mesh consisting of 12,500 hexahedral elements and the vertical tip displacement at point 'A' is 24.213 mm and the total strain energy is 12.12 Pa. The convergence of the vertical displacement at point 'A' and the convergence of the total strain energy solution is shown in Figures 15(a) and 15(b), respectively. The results from the present formulation is also compared with tetrahedral elements. It can be inferred that the both polyhedral elements and tetrahedral elements yield accurate result and converges to the reference solution asymptotically. The nodal pressure solution is shown in Figure 16(a) for polyhedral elements using VANP-CS and Figure 16(b) for tetrahedral elements using MINI, respectively. It is observed that the nodal pressure is stable within the domain for both the MINI and the proposed method.

Short cantilever. As a last example, consider a three dimensional short cantilever subjected to a uniform pressure on its upper face. The displacements (in all three directions) on the adjacent vertical face (hatched region in Figure 17(a) is constrained. The geometry and the boundary conditions of the problem are shown in Figure 17(a). A representative polyhedral mesh used in the study is shown in Figure 17(b). As approximate strain energy of 0.950930 MPa is taken as the reference solution, as reported in [48] and the reference solution for the vertical displacement at point 'A' (see Figure 17(a)) is taken as 3.312 mm as reported in [49]. This is for a Poisson's ratio $\nu = 0.25$ and Young's modulus, $E = 1$ MPa. The vertical displacement at point 'A' is estimated using Abaqus with 20,675 tetrahedral elements as 3.3 mm, 3.513 mm and 3.32 mm for different Poisson's ratio (i.e $\nu = 0.25$, 0.45, 0.4999999). Similarly, the strain energy is estimated as 0.9438 MPa, 1.0031 MPa and 0.9518 MPa for different Poisson's ratio. The convergence of the vertical displacement at point 'A' and the

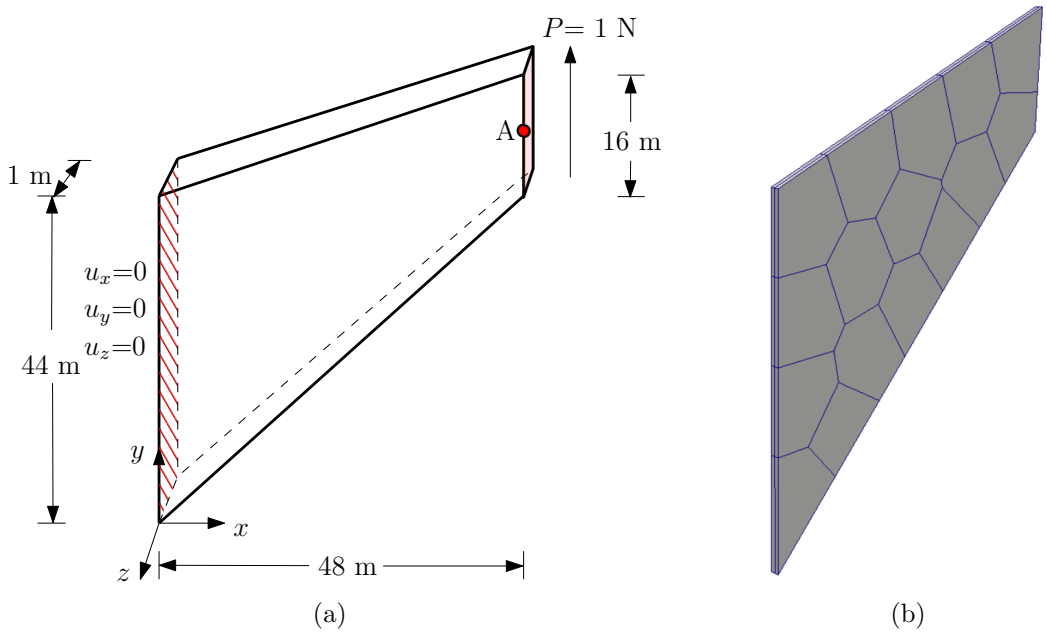

Figure 14: Cooks membrane: (a) geometry and boundary conditions (b) a sample polyhedral mesh.

total strain energy is shown in Figure 18. It can be seen that the proposed framework converges to the reference solution asymptotically.

5. Concluding Remarks

In this work, we extended the MINI element over triangles to arbitrary polytopes by employing the VANP method. The computational burden is reduced by using the strain smoothing technique. It is noted that both were originally proposed for meshfree methods. The framework presented alleviates volumetric locking and leads to a purely displacement based formulation with the nodal pressure computed at the post-processing stage. The constant strain smoothing technique is used to compute the terms in the bilinear and linear form, which significantly reduces the computational burden, without compromising accuracy. It is noted that the VANP over classical simplex element is the well known MINI element. From the numerical study, it can be inferred that the proposed framework does not suffer from volumetric locking phenomenon. The proposed method also preserves optimal convergence rates in both the L^2 norm and in the H^1 seminorm for both two and three dimensional problems.

Acknowledgements

Stéphane Bordas thanks the financial support of the European Research Council Starting Independent Research Grant (ERC Stg grant agreement No. 279578) entitled "Towards real time multiscale simulation of cutting in non-linear materials with applications to surgical simulation and computer guided surgery" and is also grateful for the support of the Fonds National de la Recherche Luxembourg FNRS-FNR grant INTER/FNRS/15/11019432/EnLightenIt/Bordas.

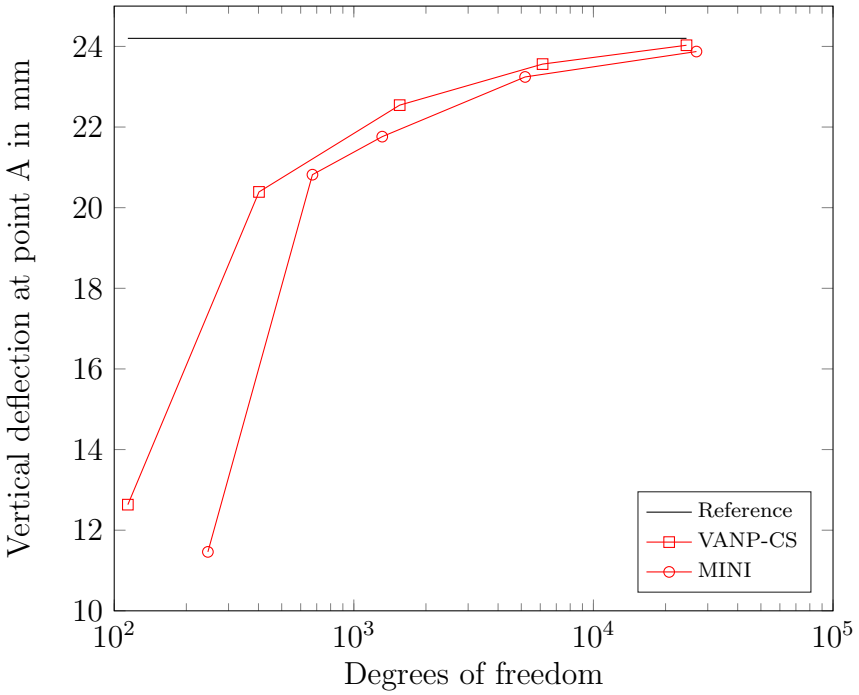

(a)

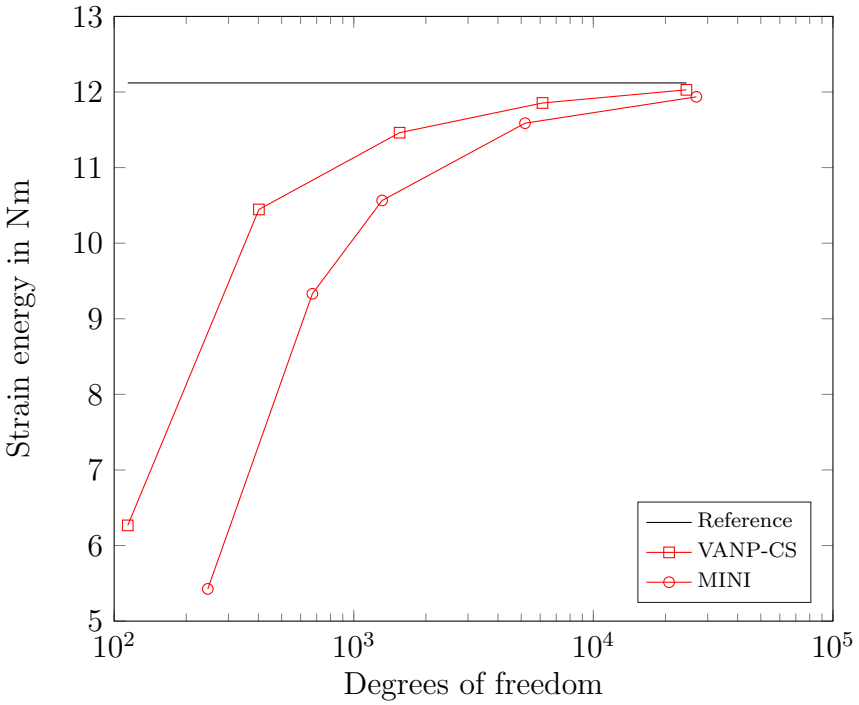

(b)

Figure 15: 3D Cooks membrane - convergence of the (a) vertical displacement (u_y) at point A and (b) total strain energy with mesh refinement for Poisson's ratio $\nu = 0.4999999$ to the reference solution.

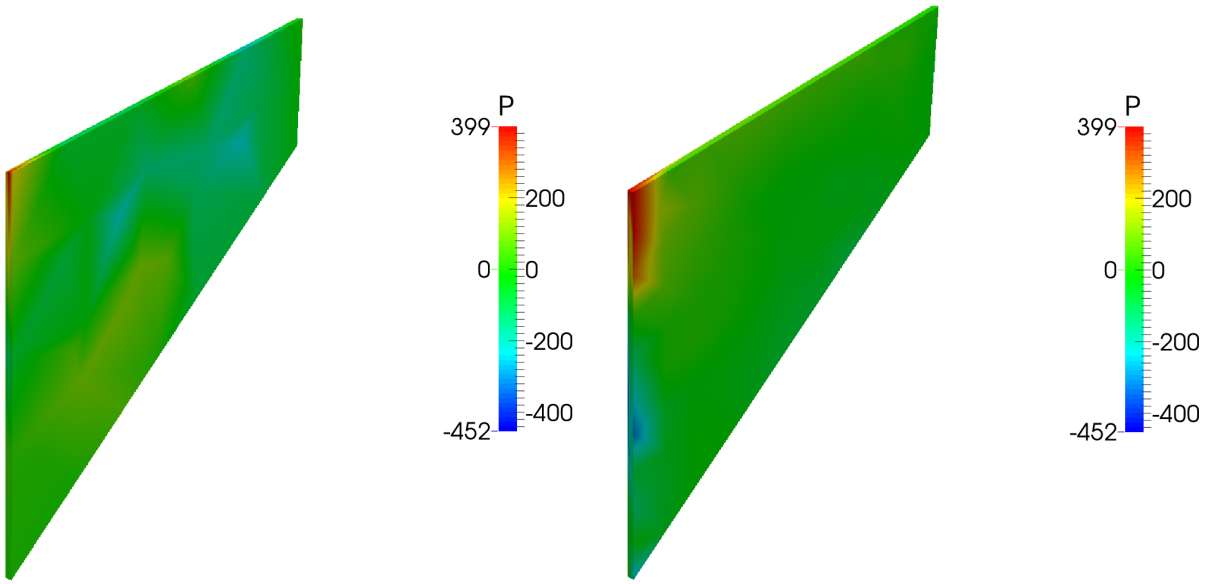

(a) (b)

Figure 16: Cooks membrane discretized with tetrahedral and polyhedral elements, respectively (a) nodal pressure for 224 polyhedral elements with 306 degrees of freedom (b) nodal pressure for 554 tetrahedral elements with 669 degrees of freedom.

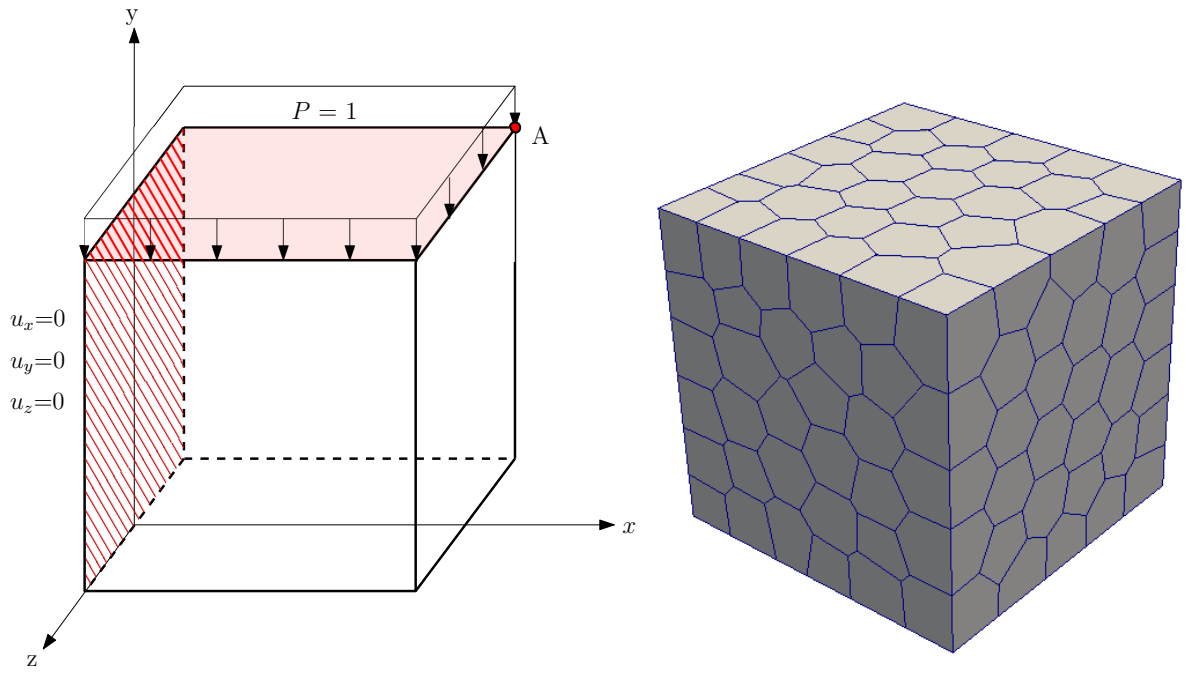

(a) (b)

Figure 17: Short cantilever: (a) Geometry and boundary conditions (b) a sample polyhedral mesh.

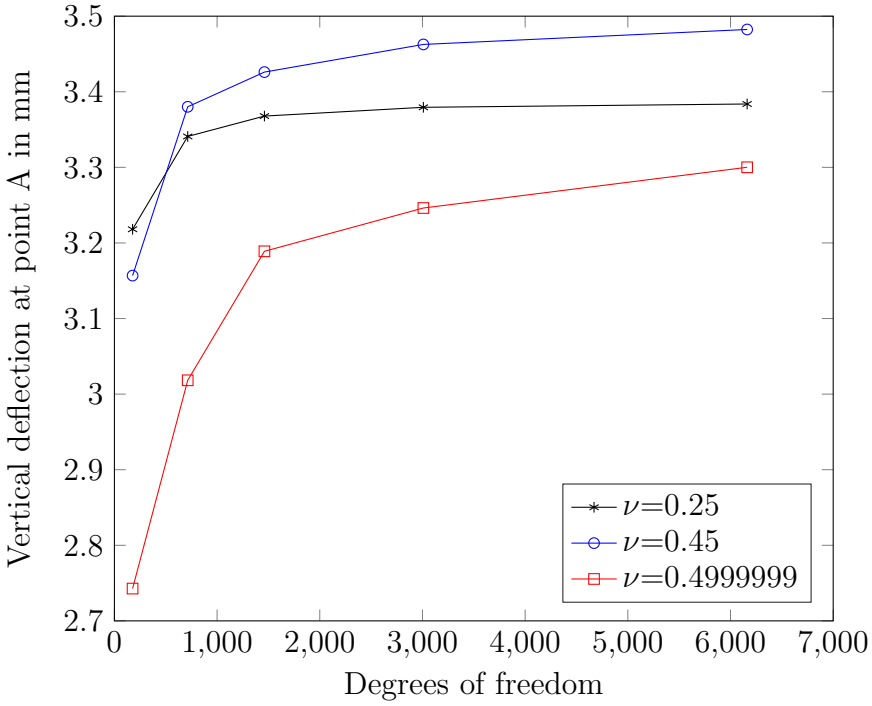

(a)

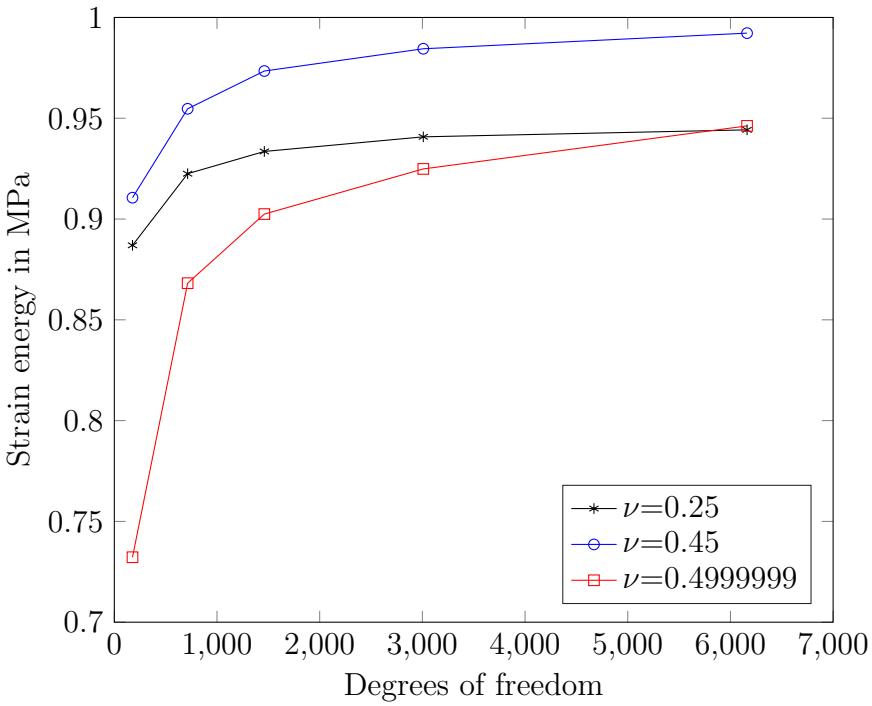

(b)

Figure 18: Short cantilever: (a) Convergence of the vertical deflection (u_y) at point 'A' and (b) convergence of the total strain energy with the mesh refinement for different Poisson's ratio i.e $\nu = 0.25$, 0.45 and 0.4999999.

Sundararajan Natarajan would like to thank MHRD and MoRTH, Government of India, for the financial support under the IMPRINT India initiative (Pr.No. MEE/1617/357 /MIMP/KRIA), and the industrial partner MRF.

References

[1] N. Sukumar, Construction of polygonal interpolants: a maximum entropy approach, International Journal for Numerical Methods in Engineering 61 (2004) 2159–2181.

[2] N. Sukumar, E. A. Malsch, Recent advances in the construction of polygonal finite element interpolants, Archives of Computational Methods in Engineering 13 (2006) 129.

[3] C. Talischi, G. H. Paulino, A. Pereira, I. F. M. Menezes, Polymesher: A general-purpose mesh generator for polygonal elements written in matlab, Structural and Multidisciplinary Optimization 45 (2012) 309–328.

[4] A. Rand, A. Gillette, C. Bajaj, Quadratic serendipity finite elements on polygons using generalized barycentric coordinates, Mathematics of Computation 83 (2014) 2691–2716.

[5] S. Nguyen-Hoang, H. Nguyen-Xuan, A polytree-based adaptive polygonal finite element for topology optimization: on an adaptive polytree mesh structure for topology optimization, International Journal for Numerical Methods in Engineering 110 (2016).

[6] J. Jaskowiec, P. Plucinski, A. Stankiewicz, Discontinuous galerkin method with arbitrary polygonal finite elements, Finite Elements in Analysis and Design 120 (2016) 1–17.

[7] B. Lévy, Robustness and efficiency of geometric programs: The predicate construction kit (PCK), Computer-Aided Design 72 (2016) 3–12.

[8] A. R. Khoei, R. Yasbolaghi, S. Biabanaki, A polygonal finite element method for modeling crack propogation with minimum remeshing, International Journal of Fracture 194 (2015) 123–148.

[9] C. Talischi, G. H. Paulino, Addressing integration error for polygonal finite elements through polynomial projections: A patch test connection, Mathematical Models and Methods in Applied Sciences 24 (2014) 1701–1727.

[10] H. Chi, C. Talischi, O. Lopez-Pamies, G. H. Paulino, A paradigm for higher-order polygonal elements in finite elasticity using a gradient correction scheme, Computer Methods in Applied Mechanics and Engineering 306 (2016) 216–251.

[11] C. Talischi, A. Pereira, G. H. Paulino, I. F. M. Menezes, M. S. Carvalho, Polygonal finite elements for incompressible fluid flow, International Journal for Numerical Methods in Fluids 74 (2014) 134–151.

[12] C. Talischi, A. Pereira, I. F. Menezes, G. H. Paulino, Gradient correction for polygonal and polyhedral finite elements, International Journal for Numerical Methods in Engineering 102 (2015) 728–747.

[13] J. S. Chen, C. Wu, S. Yoon, Y. You, A stabilized conforming nodal integration for galerkin mesh-free methods, International Journal for Numerical Methods in Engineering 50 (2001) 435–466.

[14] J. Chen, M. Hillman, M. Rüter, An arbitrary order variationally consistent integration method for galerkin meshfree methods, International Journal for Numerical Methods in Engineering 95 (2013) 387–413.

[15] D. Wang, J. S. Chen, A hermite reproducing kernel approximation for thin-plate analysis with sub-domain stabilized conforming integration, International Journal for Numerical Methods in Engineering 74 (2008) 368–390.

[16] G. R. Liu, T. T. Nguyen, D. K. Y, K. Y. Lam, Theoretical aspects of the smoothed finite element method (sfem), International Journal for Numerical Methods in Engineering 71 (2007) 902–930.

[17] S. Natarajan, E. T. Ooi, A. Saputra, C. Song, A scaled boundary finite element formulation over arbitrary faceted star convex polyhedra, Engineering Analysis with Boundary Elements 80 (2017) 218–229.

[18] A. Francis, A.Ortiz-Bernardin, S. P. A. Bordas, S. Natarajan, Linear smoothed polygonal and polyhedral finite elements, International Journal for Numerical Methods in Engineering 109 (2017) 1263–1288.

[19] A. Francis, S. Natarajan, E. A. B. Lévy, S. P. Bordas, A one point integration rule over star convex polytopes, Computers & Structures 215 (2019) 43–64.

[20] L Beirão da Veiga, F. Brezzi, A. Cangiani, G. Manzini, L. D. Marini, A. Russo, Basic principles of virtual element methods, Mathematical Models and Methods in Applied Sciences 23 (2013) 199–214.

[21] A. Gain, C. Talischi, G. H. Paulino, On the virtual element method for three-dimensional elasticity problems on arbitrary polyhedral meshes, Computer Methods in Applied Mechanics and Engineering 282 (2014) 132–160.

[22] P. F. Antonietti, M. Bruggi, S. Scacchi, M. Verani, On the virtual element method for topology optimization on polygonal meshes: A numerical study, Mathematics- Numerical Analysis (2016).

[23] H. Chi, L Beirão da Veiga, G. Paulino, Some basic formulations of the virtual element method (VEM) for finite deformations, Computer Methods in Applied Mechanics and Engineering 318 (2017) 148–192.

[24] X. hai Tang, S.-C. Wu, C. Zheng, J. hai Zhang, A novel virtual node method for polygonal elements, Applied Mathematics and Mechanics 30 (2009) 1233–1246.

[25] C. Lee, H. Kim, S. Im, Polyhedral elements by means of node/edge-based smoothed finite element method, International Journal for Numerical Methods in Engineering (2016).

[26] E. Ooi, C. Song, S. Natarajan, Construction of high-order complete scaled boundary shape functions over arbitrary polygons with bubble functions, International Journal for Numerical Methods in Engineering 108 (2016) 1086–1120.

[27] H. Talebi, A. Saputra, C. Song, Stress analysis of 3d complex geometries using the scaled boundary polyhedral finite elements, Computational Mechanics 58 (2016) 697–715.

[28] A. Cangiani, E. H. Georgoulis, P. Houston, hp-version discontinuous galerkin methods on polygonal and polyhedral meshes, Mathematical Models and Methods in Applied Sciences 24 (2014) 2009–2041.

[29] S. O. R. Biabanaki, A. R. Khoei, A polygonal finite element method for modeling arbitrary interfaces in large deformation problems, Computational Mechanics 50 (2012) 19–33.

[30] S. Biabanaki, A. R. Khoei, P. Wriggers, Polygonal finite element methods for contact-impact problems on non-conformal meshes, Computer Methods in Applied Mechanics and Engineering 269 (2014) 198–221.

[31] H. Chi, C. Talischi, O. Lopez-Pamies, G. H. Paulino, Polygonal finite elemetns for finite elasticity, International Journal for Numerical Methods in Engineering 101 (2015) 305–328.

[32] A. Ortiz, M. A. Puso, N. Sukumar, Maximum-entropy meshfree method for compressible and near-incompressible elasticity, Computer Methods in Applied Mechanics and Engineering 199 (2010) 1859–1871.

[33] A. Ortiz-Bernardin, J. Hale, C. Cyron, Volume-averaged nodal projection method for nearly-incompressible elasticity using meshfree and bubble basis functions, Computer Methods in Applied Mechanics and Engineering 285 (2015) 427–451.

[34] A. Ortiz-Bernardin, M. A. Puso, N. Sukumar, Improved robustness for nearly-incompressible large deformation meshfree simulations on delaunay tessellations, Computer Methods in Applied Mechanics and Engineering 293 (2015) 348374.

[35] C. Dohrmann, P. B. Bochev, A stabilized finite element method for the stokes problem based on polynomial pressure projections, International Journal for Numerical Methods in Fluid 46 (2004) 183–201.

[36] P. B. Bochev, C. Dohrmann, M. D. Gunzburger, Stabilization of low-order mixed finite elements for the stokes equations, SIAM Journal on Numerical Analysis 44 (2006) 82–101.

[37] J. S. Chen, P. C, A pressure projection method for nearly incompressible rubber hyperelasticity, part i: theory, Journal of Applied Mechanics 63 (1996) 862–868.

[38] J. S. Chen, S. Yoon, H. P. Wang, W. K. Liu, An improved reproducing kernel particle method for nearly incompressible finite elasticity, Computer Methods in Applied Mechanics and Engineering 181 (2000) 117–145.

[39] E. Wachspress, A Rational Finite Element Basis, volume 114, Academic Press, 1975.

[40] T. J. R. Hughes, Generlization of selective integration procedures to anisotropic and nonlinear media, International Journal for Numerical Methods in Engineering 15 (1980) 1413–1418.

[41] Q. Duan, X. Li, H. Zhang, T. Belytschko, Second-order accurate derivatives and integration schemes for meshfree methods, International Journal for Numerical Methods in Engineering 92 (2012) 399–424.

[42] Q. Duan, X. Gao, B. Wang, X. Li, H. Zhang, A four-point integration scheme with quadratic exactness for three-dimensional element-free galerkin method based on variationally consistent formulation, Computer Methods in Applied Mechanics and Engineering 280 (2014) 84–116.

[43] Q. Duan, X. Gao, B. Wang, X. Li, H. Zhang, T. Belytschko, Y. Shao, Consistent element-free galerkin method, International Journal for Numerical Methods in Engineering 99 (2014) 79–101.

[44] D. Arnold, F. Brezzi, M. Fortin, A stable finite element for the stokes equations, Calcolo 21 (1984) 337344.

[45] A. Ortiz, M. A. Puso, N. Sukumar, Maximum-entropy meshfree method for compressible and nearly incompressible elasticity, Computer Methods in Applied Mechanics and Engineering 199 (2009) 1859–1871.

[46] S. P. Timoshenko, J. N. Goodier, Theory of Elasticity, McGraw-Hill, NY, third edition, 1970.

[47] K. J. Bathe, The inf-sup condition and its evaluation for mixed finite element methods, Computers and Structures 79 (2001) 243–252.

[48] O. J. B. A. Pereira, Hybrid equilibrium hexahedral elements and super-elements, Communications in Numerical Methods in Engineering 24 (2008) 157–165.

[49] G. R. Lui, T. Nguyen-Thoi, Smoothed Finite Element Methods, CRC Press (Taylor and Francis), 2010.